Journal of the European Ceramic Society 46 (2026) 118317

Contents lists available at ScienceDirect

Journal of the European Ceramic Society

journal homepage: www.elsevier.com/locate/jeurceramsoc

Impact of sintering temperature on structural, microstructural and electrical properties of screen-printed $0.7Pb(Fe_{0.5}Nb_{0.5})O_3–0.3BiFeO_3$ thick films

Ivana Goričan [a,b], Andreja Benčan [a,b], Silvo Drnovšek [a], Antonio Iacomini [a], Nejc Suban [a,b], Brigita Kmet [a], Uroš Prah [a,1], Tadej Rojac [a,b], Hana Uršič [a,b,*]

[a] Electronic Ceramics Department, Jožef Stefan Institute, Jamova cesta 39, Ljubljana 1000, Slovenia
[b] Jožef Stefan International Postgraduate School, Jamova cesta 39, Ljubljana 1000, Slovenia

ARTICLE INFO

Keywords:
Thick film
Screen printing
Multiferroic
PFN–BFO
Linear thermal expansion coefficient

ABSTRACT

$(1–x)Pb(Fe_{0.5}Nb_{0.5})O_3–xBiFeO_3$ (PFN–100*x*BFO) ceramics exhibit versatile functional properties, from ferroelectric, relaxor to antiferroelectric behaviour, but have not yet been prepared as ceramic thick films, which are the key to miniaturization of electronic components. In this work, screen-printed thick films of PFN–30BFO were prepared on gold-coated alumina substrates and sintered at 800 °C, 850 °C and 930 °C. The impact of the sintering temperature on their properties was studied. The films annealed at 930 °C exhibited excessive electrical conductivity. In contrast, well developed polarization versus electric field hysteresis loops were observed in the films treated at 800 °C and 850 °C. The films annealed at 800 °C had the smallest grain size and dielectric permittivity values but achieved the highest dielectric breakdown strength. The findings of this study highlight the potential of PFN–30BFO screen-printed films, sintered at 800 °C, for use in miniaturized high-voltage electronic devices.

1. Introduction

Thick-film technologies are powder-based technologies that enable the preparation of films with typical thicknesses between one and a few hundred micrometres. They allow the miniaturization of electronic components and direct deposition of films on various substrates. The most widely used thick-film method is screen printing, which is also suitable for ceramic materials. In this technique, a thick film paste composed of ceramic powder and organic binders is pressed through a screen onto the substrate to produce a thick green film, which is then densified at a high temperature, usually above 900 °C. Screen printing is particularly advantageous as it enables the production of a wide range of materials, including insulators such as dielectrics, semiconductors and conductors, e.g. metal electrodes [1–3].

$Pb(Fe_{0.5}Nb_{0.5})O_3$ (PFN), which crystallizes in monoclinic symmetry with space group *Cm* [4–6], and $BiFeO_3$ (BFO) ceramics, which crystallizes in rhombohedral symmetry with space group *R*3*c* [7–9] are well-known single-phase multiferroic materials. The scientific community has also shown considerable interest in the properties of their solid solutions, namely $(1−x)Pb(Fe_{0.5}Nb_{0.5})O_3–xBiFeO_3$ (PFN–100*x*BFO) [4,9–11]. The addition of BFO to PFN gradually leads to the formation of a pseudocubic symmetry indexed with space group *Pm*-3*m*, which results in enhanced relaxor-like characteristics of the materials. In compositions with a BFO content of $x = 0.05–0.1$, a pseudocubic and a monoclinic phase coexist. However, when the BFO content is $0.2 \leq x \leq 0.5$, only a pseudocubic phase is present [4]. A transition to rhombohedral symmetry occurs in compositions where the BFO content is $x > 0.6$ [7,9].

Unlike the canonical relaxor $Pb(Mg_{1/3}Nb_{2/3})O_3$ [12], unmodified PFN exhibits a weakly-frequency dependent peak-permittivity temperature for frequencies below 1 MHz [13,14]. In contrast, PFN–10BFO and PFN–20BFO show a more pronounced relaxor behaviour with a permittivity peak near room temperature (RT), making them promising candidates for caloric applications [4]. A further study confirmed that PFN–20BFO-based ceramics exhibit excellent electrocaloric and magnetocaloric properties, resulting to be one of the best single-phase multicaloric materials. For PFN–20BFO doped with 0.5 mol% Mn, the maximum electrocaloric temperature change (ΔT_{EC}) of 1.8 °C was observed at 76 °C. The magnetocaloric temperature change (ΔT_{MC}) was

* Corresponding author at: Electronic Ceramics Department, Jožef Stefan Institute, Jamova cesta 39, Ljubljana 1000, Slovenia.
E-mail address: hana.ursic@ijs.si (H. Uršič).
[1] Present address: Luxembourg Institute of Science and Technology, 4362 Esch-sur-Alzette, Luxembourg.

https://doi.org/10.1016/j.jeurceramsoc.2026.118317
Received 5 December 2025; Received in revised form 9 March 2026; Accepted 16 March 2026
Available online 17 March 2026

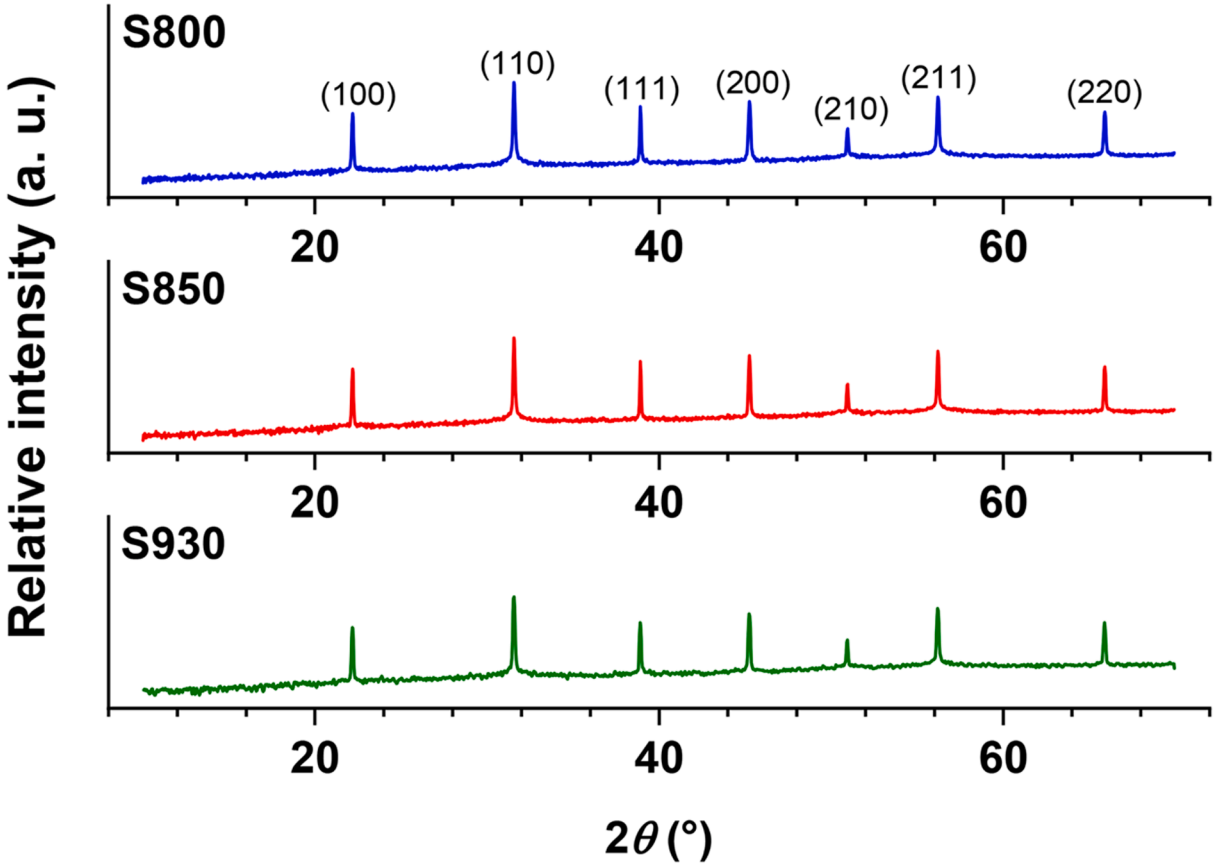

Fig. 1. Comparison of XRD patterns of S800 (blue solid line), S850 (red solid line) and S930 films (green solid line) in the 2θ range of 10–70°. To illustrate the absence of secondary phases, the intensities are expressed on a logarithmic scale.

found to be 0.15 °C at –270 °C. Further doping with 12 mol% Gd additionally improved the ΔT_{MC} and reached a maximum of 2.2 °C at –270 °C [15].

For the compositions with higher BFO content ($0.3 \leq x \leq 0.5$), the frequency and temperature dependence of the permittivity exhibits increased complexity compared to PFN–20BFO, i.e., more than one peak appears in the dielectric permittivity versus temperature curve. An increased electrical conductivity is observed at elevated temperatures. The *P–E* hysteresis loops are observed to be pinched, for which there are several possible contributions. It could be related to the reorganization of the polar nanoregions under the applied electric field, which could induce a transition between the ferroelectric and the relaxor phase. Additionally, the pinching might arise from antiferroelectric ordering and/or the presence of charged point defects acting as pinning centres [4].

The *P–E* hysteresis loops of the PFN–60BFO and PFN–70BFO ceramics show ferroelectric behaviour. Compared to the compositions with a BFO content of $0.3 \leq x \leq 0.5$, the frequency and temperature dependence of the dielectric permittivity becomes less complex with only one observed permittivity peak [16]. Pure BFO exhibits an electrically conductive ferroelectric *P–E* hysteresis loop, which is reported in the literature as either pinched [17] or more open [18] depending on the state of the charged defects. It has been reported that rapid cooling in water from $T > T_c$ leads to the opening of the hysteresis loop [17]. As expected, the aforementioned increased electrical conductivity is also reflected in enhanced dielectric losses [19].

Besides relaxor-ferroelectric properties, PFN exhibits antiferromagnetic properties, which upon heating above approximately –120 °C transition to the paramagnetic state. The temperature of this transition is known as a Néel temperature (T_N) [20,21]. The addition of BFO increases the T_N of the ceramics. In compositions with a BFO content of $x < 0.1$, below T_N the antiferromagnetic phase is still observed. In compositions with BFO content of $0.1 \leq x \leq 0.2$, depending on the temperature, two different types of ferromagnetic states are observed, while for compositions with $x \geq 0.25$, the system transitions back to an antiferromagnetic state [10]. For pure BFO, the T_N is approximately 370 °C [22].

Despite the promising and intriguing features for functional applications, thick films of PFN–100*x*BFO ($0 < x < 1$) prepared using a powder-based technologies have not yet been reported. Besides the bulk ceramic samples, only the properties of PFN–5BFO single crystals [23] and PFN–50BFO thin films prepared by the RF-cathode sputtering method [24] have been studied so far. In this work, we investigated the structural, microstructural, dielectric and ferroelectric properties of PFN–30BFO thick films prepared by the screen-printing method. The thick-film paste was screen printed on gold-coated alumina substrates and thermally treated at 800 °C, 850 °C and 930 °C. Among the films, those sintered at 800 °C were found to be the most promising for potential applications in electronic devices.

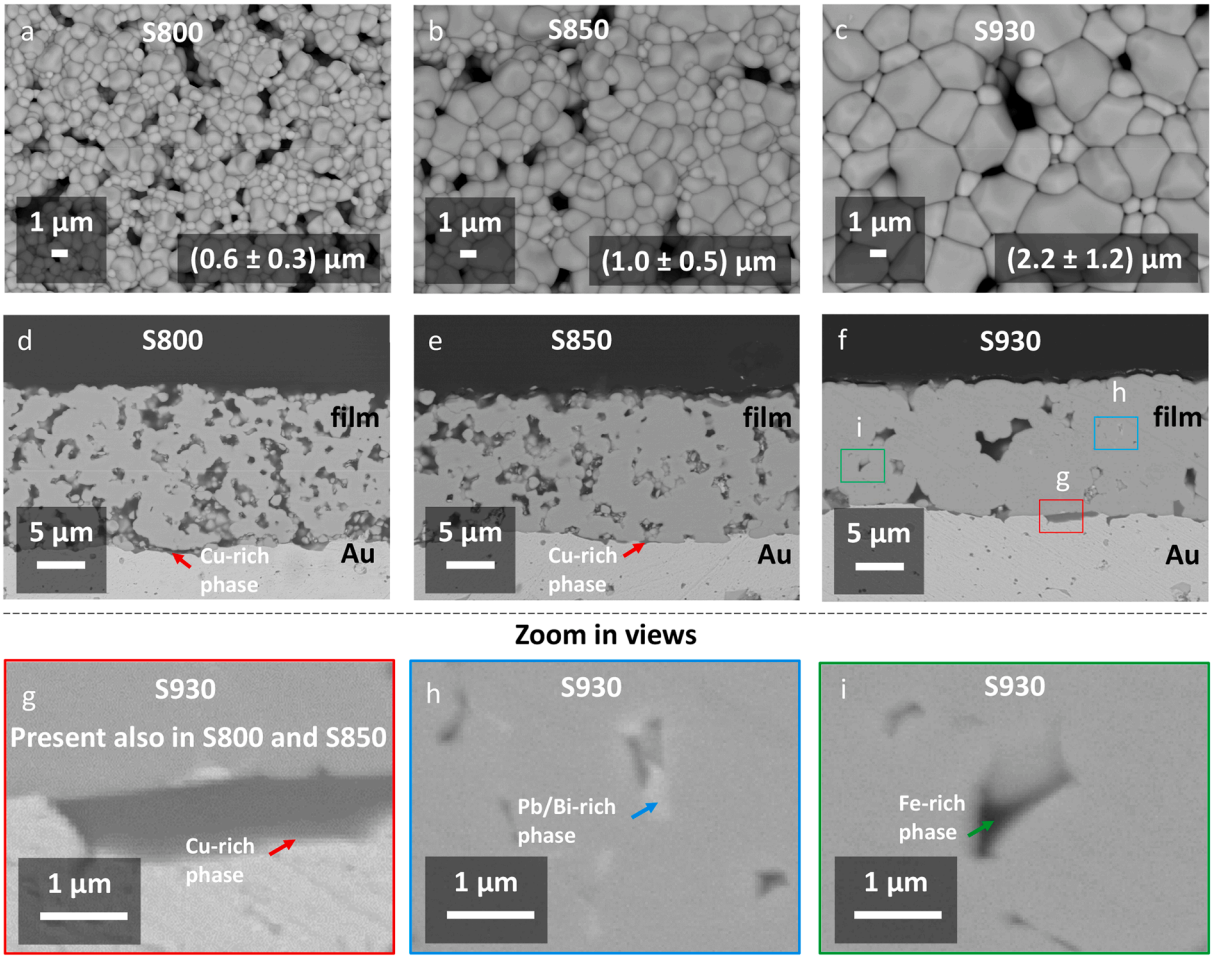

Fig. 2. SEM microstructures of (a)–(c) surfaces and (d)–(f) cross-sections of S800, S850 and S930 films. In (f), the visible secondary phases are marked with rectangles. Zoomed-in views of these secondary phases (g)–(i) reveal a Cu-rich phase (marked in red), a Pb/Bi-rich phase (marked in blue) and a Fe-rich phase (marked in green), respectively. For better visualisation, only the Cu-rich phase of the S930 film is enlarged; however, this secondary phase is also observed in the S800 and S850 films.

2. Materials and methods

The PFN–30BFO powder was prepared by mechanochemical synthesis using PbO (99.9%, Alfa Aesar, Germany), Fe_2O_3 (99.9%, Alfa Aesar, Germany), Nb_2O_5 (99.9%, Aldrich, Germany) and Bi_2O_3 (99.999%, Alfa Aesar, Germany). The stoichiometric starting oxide mixture was homogenized in a planetary ball mill at 200 min^{-1} for 4 h in ethanol using yttria-stabilized zirconia (YSZ) balls. After drying, it was mechanochemically activated in the same mill for 14 h at 400 min^{-1} in a tungsten carbide container with tungsten carbide balls. The activated mixture was then milled again in ethanol at 200 min^{-1} for 4 h using YSZ balls. Details on the preparation of the powder can be found in the reference [4]. The powder was additionally heated to 800 °C for 1 h. The thick-film paste was prepared by mixing the PFN–30BFO powder with an organic vehicle consisting of alpha-terpineol (≥98%, Merck, Germany), 2–2-butoxy-ethoxy-ethyl acetate (≥ 98%, Merck, Germany) and ethyl cellulose (48% ethoxyl, Sigma Aldrich, USA) in a mass ratio of 60:25:15 [25].

The 3-mm-thick Al_2O_3 substrates were prepared by the slip casting from Alcoa A-16. The substrates were then sintered at 1600 °C for 4 h. In the next step, the $PbZr_{0.53}Ti_{0.47}O_3$ (PZT) barrier layer was printed on the top of the substrates and thermally treated at 500 °C for 1 h to evaporate the organic compounds and additionally sintered at 1100 °C for 2 h, as explained in [25]. The barrier layer was prepared to minimize possible chemical interactions between the substrate and the functional layers, as suggested in [25,26]. Finally, the thick-film Au paste (8884-G, ESL, USA) was printed on the PZT layer and thermally treated at 850 °C for 1 h as suggested in [27].

The PFN–30BFO thick-film paste was printed twice on the Au/PZT/Al_2O_3 substrates. Intermediate drying for each printing step was carried out at 150 °C for 15 min. The prepared samples were then thermally treated at 600 °C for 1 h to remove an organic vehicle. The thickness of the prepared samples was 15 µm. Finally, the samples were annealed at 800 °C, 850 °C and 930 °C for 2 h in an oxygen atmosphere and in the presence of the $Pb(Fe_{0.5}Nb_{0.5})O_3$ packing powder. Further in the text, these films are referred to as S800, S850 and S930, respectively.

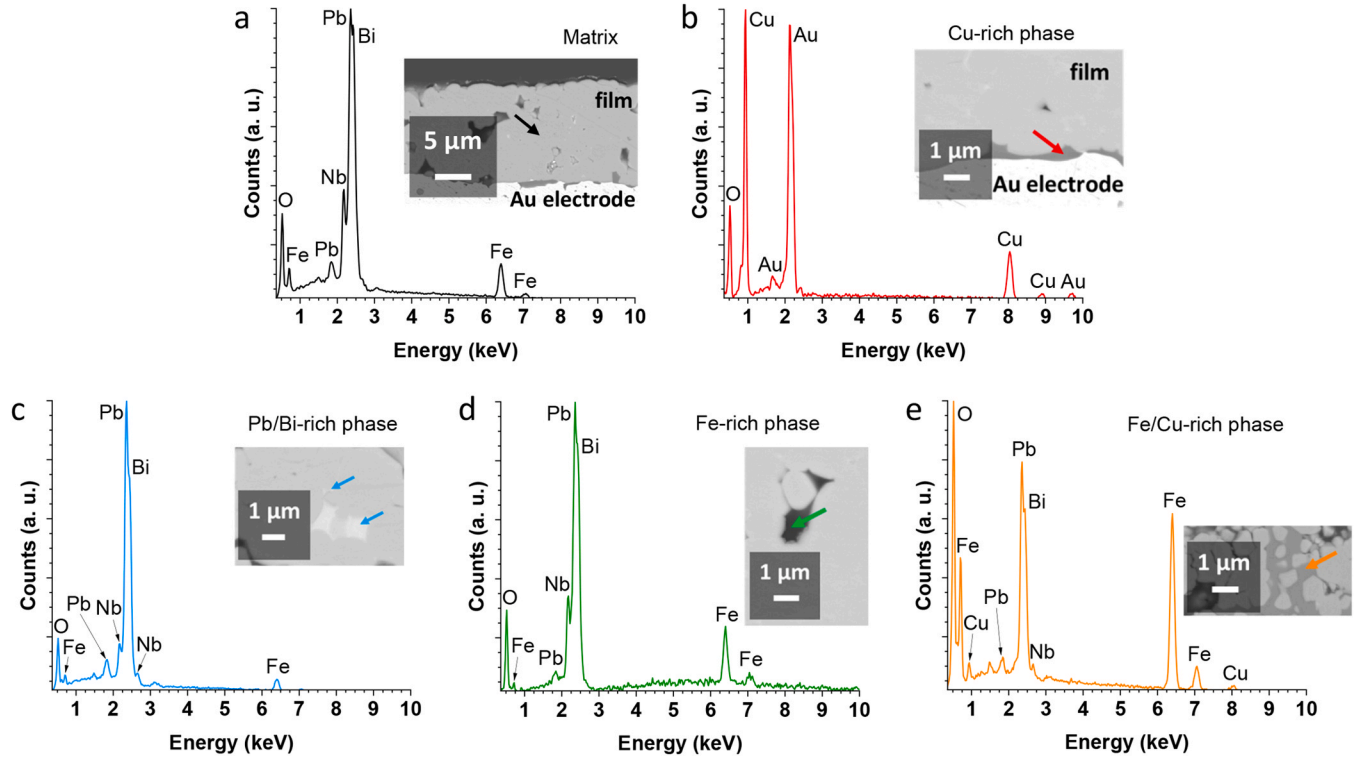

Fig. 3. EDXS spectra of the S930 films, namely (a) matrix, (b) Cu-rich phase, (c) Pb/Bi-rich phase, (d) Fe-rich phase and (e) Fe/Cu-rich phase.

The PFN–30BFO powder and the thick films were analysed with the X-ray diffractometer (XRD, X'Pert PRO, PANalytical, Netherlands) using Cu-Kα_1 radiation in the 2θ range of 10°–70°. The step size of the measurements was 0.034° and the time of the steps was 100 s. Phase identification was performed using the PDF-4+ database. Since the PDF card of PFN–30BFO is not available, the PDF cards of PFN (no. 00-066-0292, *Cm* space group [28]) and PFN–60BFO (no. 04-018-7360, *Pm*-3*m* space group [29]) were used. The XRD peaks of the prepared thick films were also compared with the perovskite peaks of the PFN–30BFO bulk ceramics reported in [4]. Structural determinations were carried out using the MAUD program (Multiple Analysis Using Diffraction) through the Rietveld refinement method [30].

The microstructures of the surfaces and cross-sections of the samples were analysed using a field-emission scanning electron microscope (FE-SEM, JSM 7600F, Jeol Ltd., Japan) equipped with an energy dispersive X-ray spectrometer (EDXS, Inca Oxford 350 EDS SSD, Oxford Instruments, U.K.). The spectra were acquired at 15 keV. The cross-section samples were mounted in epoxy resin and polished prior to analysis. The average grain size was estimated from the SEM images of the sample surfaces. For the analysis, Feret diameters [31] of ~300 grains were determined using Image Tool software (UTHSCSA Image Tool Version 3.00. 2002) [32]. The porosity of the films was estimated from their cross-sections using Image Tool software. Three different images were analysed for each film.

The topography and root-mean-square surface roughness (R_q) of the samples were analysed using an atomic force microscope (AFM, MFP-3D, Asylum Research, USA). Images were acquired in AC air topography mode using a Pt-coated Si tip (OMCL-AC240TM-R3, Olympus, Japan). Local electrical conductivity was investigated using a conductive AFM (cAFM) module (ORCA module). Measurements were performed by applying a DC voltage of 7 V between the conductive tip and the bottom Au electrode. Piezoresponse force microscopy (PFM) was performed in dual-ac resonance tracking (DART) mode by atomic force microscope (AFM, Jupiter XR, Asylum Research, USA). A Ti/Pt-coated Si tip (OMCL-AC240TM-R3, Olympus, Japan) was used for the measurements. A voltage signal with an amplitude of 0.1 V and 2 V and a frequency of 290–300 kHz was applied to the samples.

For the electrical measurements, Au top electrodes with a diameter of 0.5 mm were deposited on the surface of the thick films by RF magnetron sputtering (5 Pascal, Trezzano sul Naviglio, Italy). The dielectric permittivity (ε') and dielectric losses (tgδ) were determined using the HP 4284A precision LCR impedance meter (Hewlett-Packard, USA). The measurements were performed at frequencies of 1–100 kHz during cooling from 200 °C to –50 °C. For the measurements of the AC current density versus electric field (*J*–*E*), the aixACCT TF analyser 2000 (aixACCT Systems GmbH, Germany) was used. Polarization versus electric field (*P*–*E*) hysteresis loops were automatically obtained by the integration of current signal. These measurements were performed at RT with a sinusoidal waveform at 100 Hz and an *E* of up to 200 kV·cm^{-1} for the S850 and S930 films and up to 350 kV·cm^{-1} for the S800 films. The aixACCT TF analyser 2000 with the Breakdown measurements mode was used for the determination of the dielectric breakdown strength (DBS). The DBS was determined by applying an increasing DC voltage signal with a step of 1.5 V and a duration of 1 s for each step. Ten Au electrodes of each sample were measured and the Weibull distribution [33–35] was used to evaluate the results.

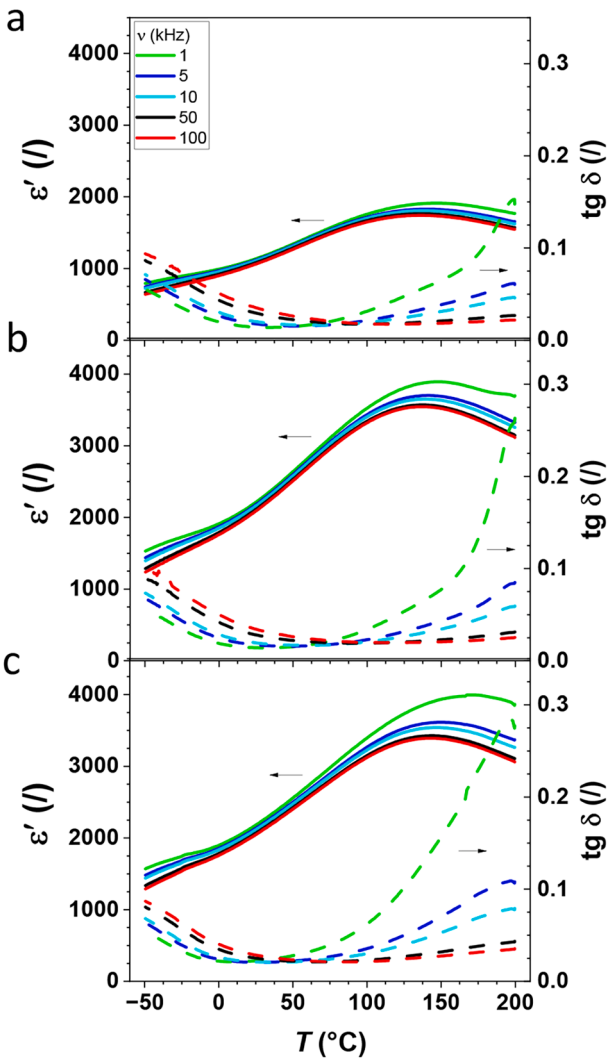

Fig. 4. Frequency and temperature dependence of ε' (solid lines) and tgδ (dashed lines) of (a) S800, (b) S850 and (c) S930 films.

The linear thermal expansion coefficient (α) of the PFN–30BFO was determined using a bulk ceramic cylinder with a diameter of $2r = 6.3$ mm and a length of 12.8 mm. The measurement of the sample expansion as a function of temperature was carried out with a dilatometer (DIL 402EP, Netzsch, Germany) in the temperature range of 100–560 °C with a step of 5 K·min^{-1}. The α value of a material is reported for the cooling cycle.

3. Results and discussion

The comparison of the XRD patterns of the S800, S850 and S950 films is shown in Fig. 1. In the XRD patterns of all samples, only the peaks belonging to the perovskite phase are visible and no additional peaks belonging to the secondary phases are detected. The Rietveld refinement analysis shows that all thick films exhibit pseudocubic symmetry indexed with space group *Pm*-3*m*, similar to the PFN–30BFO bulk ceramics [4]. Details can be found in Supplementary material A.

The SEM microstructures of the surfaces of the S800, S850 and S930 films are shown in Fig. 2(a–c). Due to the lowest sintering temperature among the samples, the average grain size of the S800 is the smallest, namely (0.6 ± 0.3) μm. The grain size of the samples increases with increasing sintering temperature and is (1.0 ± 0.5) μm and (2.2 ± 1.2) μm for the S850 and S930 films, respectively. The cross-sections of the films in Fig. 2(d–f) show that there are no microstructural gradients through the film thickness; for example, the pores are homogeneously distributed across the cross-sections. Furthermore, a comparison of the grain size determined from the film surface and the thermally-etched cross-section was performed. The results reveal a homogeneous distribution of different grain sizes through the film thickness, providing further evidence for the absence of any microstructural gradients. Details can be found in Supplementary material B. The porosity of the samples is estimated to be 7%, 6% and 2% for S800, S850 and S930 films, respectively. The R_q value of the thick films increases slightly with increasing grain size and is, on average, 207 nm, 215 nm and 240 nm for S800, S850 and S930 films, respectively. Details can be found in Supplementary material C.

The SEM images of the cross-section of the thick films shown in Fig. 2 (d–f) reveal the presence of secondary phases, which are enlarged in Fig. 2(g–i). In order to investigate their chemical composition, the thick-film matrix and the secondary phases were examined by EDXS analysis, as shown in Fig. 3. In the EDXS spectrum of the matrix (Fig. 3(a)), the peaks belonging to the Pb, Fe, Nb, Bi and O elements can be clearly observed. Since the spectra of the matrix of the S800, S850 and S930 films are comparable, only one spectrum is shown. The spectra of all thick films are shown in Supplementary material D. Furthermore, as explained below, a common secondary phase rich in Cu appears in all the films, while additional secondary phases may be observed in the S930 film.

In all thick films a secondary phase is observed at the interface between the Au electrode and the functional layer. The EDXS spectrum of the secondary phase (Fig. 3(b)) shows the presence of Cu and Au elements. The Au peaks can be attributed to the close proximity of an investigated secondary phase to the Au electrode. The secondary phase is therefore referred to as a Cu-rich phase (marked in red in Fig. 2(d–f), with a detailed zoomed-in view shown in Fig. 2(g)). Cu was found to be the main impurity in the commercially available electrode paste that we used (Au 8884-G, ESL, USA). A secondary phase rich in Cu was also observed in BFO thick films on Au/Al_2O_3 substrates [36].

Three additional secondary phases are observed in cross-sections of S930 films. The first one is visible as bright areas and inclusions at the grain boundaries (marked by the blue rectangle in Fig. 2(f) with a zoomed-in view in Fig. 2(h)), suggesting the formation of the liquid phase. From the EDXS spectrum (Fig. 3(c)), it can be seen that the phase is rich in Pb/Bi elements; therefore, from now on, referred to as a Pb/Bi-rich phase. This liquid phase is most likely a eutectic mixture of PbO and Bi_2O_3. According to the phase diagram [37], the temperature of its formation is 635 °C. This means that some of the phase could also have formed in the S800 and S850 films, but the amount is not high enough to be detected in these two samples. The EDXS spectrum of the second secondary phase (marked by the green rectangle in Fig. 2(f) with a zoomed-in view in Fig. 2(i)), can be seen in Fig. 3(d). The results show that the phase is rich in Fe; therefore, it is further referred to as a Fe-rich phase. The third secondary phase is visible only in some parts of the S930 films (not visible in Fig. 2(f)). It is shown in Fig. 3(e) with the results of its EDXS analysis. The phase is rich in Fe, but also contains Cu (from now on, referred to as a Fe/Cu-rich phase). Other elements can

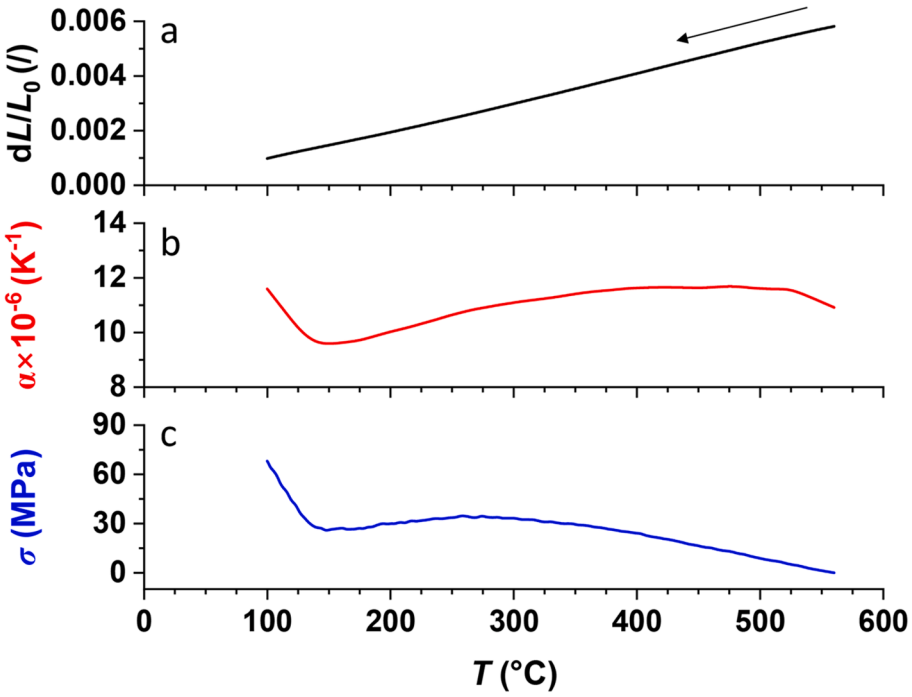

Fig. 5. Temperature dependence of (a) the dilatometric cooling curve dL/L_0, (b) the calculated α values of the PFN–30BFO ceramic and (c) the thermal stresses in PFN–30BFO thick films formed during the sintering process. The arrow indicates the direction of the measurement.

also be observed in the spectrum, namely Pb, Bi, O and a small amount of Nb. This could be due to their presence in this secondary phase, or due to the proximity of the film matrix.

The secondary phases observed in the cross-sections of the thick films in Fig. 2 were not detected by the XRD technique, as shown in Fig. 1. According to the calculations in the HighScore Plus program, the penetration depth of the X-rays (incident angle between 10° and 70°) reaches up to ~ 8 μm in depth. The thick films used in this work have a thickness of 15 μm, so the penetration depth of the X-rays is only about half the film's thickness. Since the secondary phases are present in small quantities and are not segregated in the upper part of the thick films, they do not contribute to the XRD diffractions. Another possible explanation for the absence of secondary phases in the XRD results is that these phases may exist in an amorphous state and/or in quantities below the detection limit of XRD, or may be localised at the grain boundaries [38].

The frequency and temperature dependence of ε' and tgδ of S800, S850 and S930 films are shown in Fig. 4. The permittivity peaks are broad and frequency dependent. As frequency increases, the magnitude of the permittivity values decreases. In all samples, however, as frequency increases, the peak permittivity temperatures ($T_{\varepsilon,\max}$) shift towards lower values, not higher values, which is expected for canonical relaxor behaviour [12]. The inverse relationship between $T_{\varepsilon,\max}$ and frequency (f) form that is expected for relaxors is rare but has already been reported for other materials. For example, Ref. [39] reports such behaviour for $Na_{0.5}Bi_{0.5}TiO_3$-based ceramics. Despite lacking explanations, it can be observed in that study that the apparent inverse $T_{\varepsilon,\max}$-versus-f relation occurs in the temperature region where electrical conductivity starts to dominate the dielectric response. Furthermore, in Ref. [40], this particular dielectric relaxation behaviour in $BaTi_{0.85}Zr_{0.15}O_3$-based ceramics is linked to the presence of inhomogeneous distribution of local electrical conductivity between grains and grain boundaries, which typically leads to dielectric Maxwell-Wagner effects and a positive temperature coefficient of resistivity (PTCR). Similar unusual dielectric behaviour has also been observed in spinel Cu-ferrites, where it has been attributed to the similarity between the mechanisms of polarization and electrical conduction [41]. While the exact origin of the shift of $T_{\varepsilon,\max}$ to lower temperatures with increasing frequency for the thick films studied here is still unknown, based on the presented literature cases it is likely associated with an emerging effect involving electrical conduction. Furthermore, it should be also noted that the $T_{\varepsilon,\max}$ values of all films are lower than those of relaxor-like PFN–30BFO bulk ceramic at all frequencies [4]. The depletion of the dielectric permittivity most likely arises from a combination of at least two effects. Firstly, it could be attributed to the presence of a Cu-rich secondary phase at the film-substrate interface. Such an interfacial secondary phase may act as a series electrical element, resulting in a reduction of the measured dielectric permittivity. At the same time, the observed behaviour could also be attributed to residual stresses in the films. The maximum ε' values of the thick films reach 1910, 3890 and 3980 for the S800, S850 and S930 films, respectively, at 1 kHz. A decrease in maximum permittivity values among the samples can also be attributed to the decreasing grain size. As the S800 films have the smallest grain size, they exhibit the lowest permittivity values, while the highest values are observed for films with the largest grain size, namely the S930 films. This is consistent with the literature, which shows that grain size strongly affects the electrical properties of ferroelectric ceramic materials [42–48].

The tgδ values are 0.01, 0.01 and 0.02 at room temperature and 1 kHz for S800, S850 and S930 films, respectively. The differences in the tgδ values of the thick films become more pronounced above 100 °C, which is related to the thermally activated electrical conductivity of the

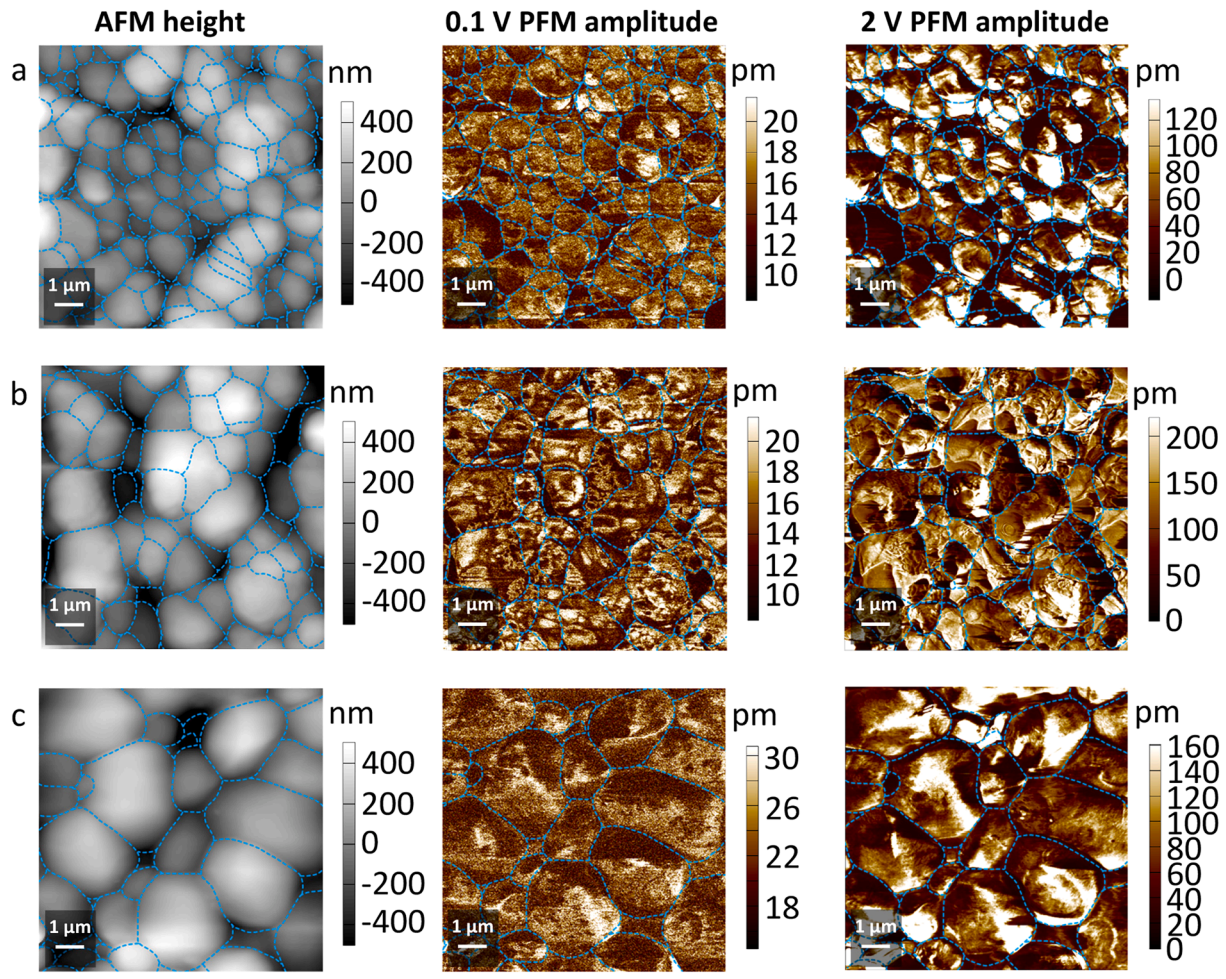

Fig. 6. AFM topography height (first column) and out-of-plane PFM amplitude images obtained at 100 mV (second column) and 2 V (third column) for (a) S800, (b) S850 and (c) S930 films. For better visualisation, the grain boundaries are outlined with blue dashed lines.

films. It can be observed that the S800 films have the lowest tgδ values among the thick films, while the tgδ values of the S930 films are the highest. It is worth noting, that the tgδ values for all thick films remain below 0.3 even at temperatures as high as 200 °C. In comparison, the tgδ values in the PFN–30BFO bulk ceramic are significantly higher at this temperature, indicating a lowered conductivity in films with respect to bulk samples [4].

The aforementioned residual stresses in the films are formed during the cooling part of the thermal treatment, which is due to the mismatch of the thermal expansion coefficient (α) between the film and the substrate [49]. This has been previously reported for various materials [25, 50–53]. The α value of PFN–30BFO is not yet reported in the literature, so we performed the dilatometric measurements to determine it. The temperature dependence of a dilatometric cooling curve is shown in Fig. 5(a). The dL/L_0 value decreases with decreasing temperature. The corresponding $\alpha(T)$ values (Fig. 5(b)) of the material reach their minimum at ~150 °C, which corresponds to the materials permittivity anomaly [4]. At temperatures below 150 °C, the $\alpha(T)$ values increase steeply. Details on the calculation of the α values from the dilatometric curve can be found in Supplementary material E. The average α value of PFN–30BFO was determined to be $\sim 11 \cdot 10^{-6}$ K^{-1} (in the temperature range 100–560 °C). According to the literature, the α value of α-Al_2O_3 is reported to be $\sim 8 \cdot 10^{-6}$ K^{-1} (in the temperature range 40–l000 °C) [54]. The α values of PFN–30BFO are higher than the α values of the substrate in the whole measured temperature range, which means that tensile stresses are formed during the cooling process [55]. The magnitude of the stresses as a function of temperature is shown in Fig. 5(c). The stress magnitude reaches a maximum value of ~70 MPa. Details on the calculation of the stresses can be found in Supplementary material F.

PFM was used to investigate the local domain structure of films at RT. The results are shown in Fig. 6. At 0.1 V, the domains in all films are small and not completely formed, resembling clusters of polar nanoregions as previously reported for other materials with relaxor-like features [56–58], including PFN–30BFO bulk ceramic [4]. At higher applied voltages, namely 2 V, the ferroelectric domains are formed. The higher magnification of PFM amplitude images is shown in Fig. 7. In all films, a few hundred to a few tens of nanometres large wedge-like domains (marked by dashed red arrows) and irregularly shaped domains (marked by solid yellow arrows) are observed. In addition, residuals of clusters of polar nanoregions are still present (marked by green

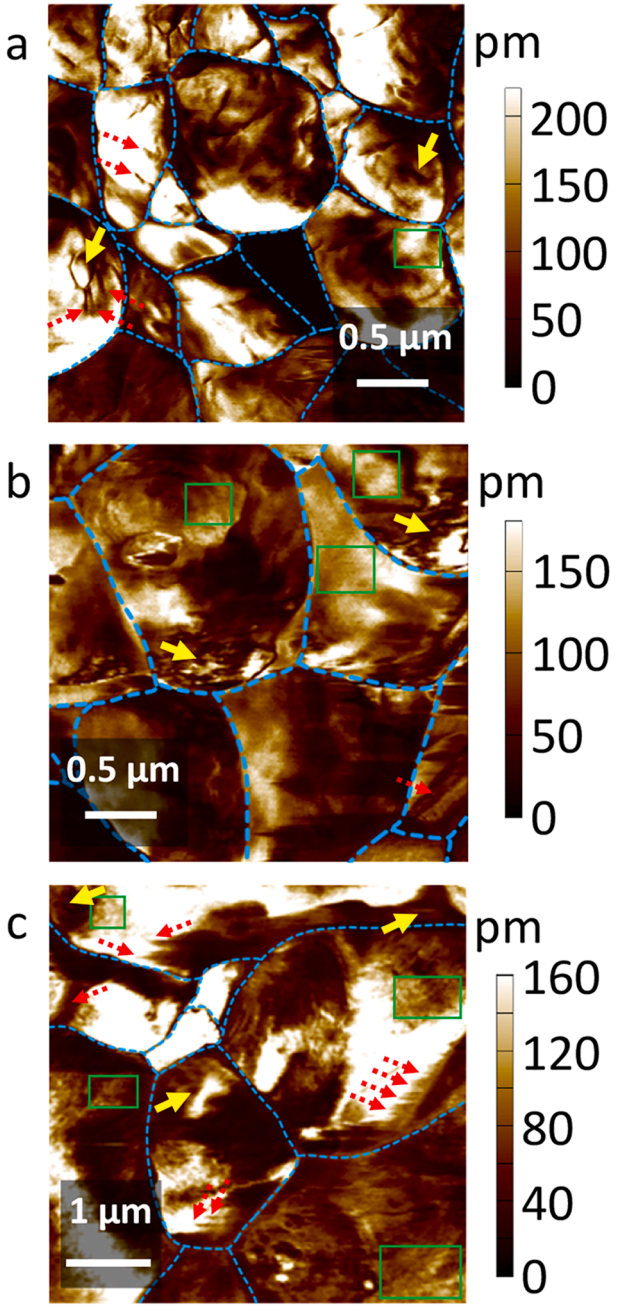

Fig. 7. High magnification PFM amplitude images obtained at 2 V for (a) S800, (b) S850 and (c) S930 films. Irregularly shaped and wedge-like domains are marked by solid yellow and dashed red arrows, respectively. The clusters of polar nanoregions are marked by green rectangles. For better visualisation, the grain boundaries are outlined with blue dashed lines.

rectangles). The out-of-plane PFM phase images can be found in Supplementary material G.

The most pronounced difference in the results of the electrical measurements between the films can be seen in the *P–E* hysteresis loops. The bipolar *P–E* and *J–E* hysteresis loops of the S800, S850 and S930 films are shown in Fig. 8. The loops of the S800 and S850 films are slim and appear to be slightly pinched (Fig. 8(a, b)), which is also supported by the *J–E* (Fig. 8(d, e)) loops that reveal a splitting of peaks (marked by red arrows). The pinching and splitting of the *P–E* and *J–E* loop were also previously observed in the PFN–30BFO bulk ceramic [4]. The *P–E* hysteresis loops of S930 films (Fig. 8(c)) are round, indicating enhanced electrical conductivity in comparison with S800 (Fig. 8(a)) and S850 films (Fig. 8(b)). Due to this, the pinching is not clearly observed, but the *J–E* loops (Fig. 8(f)) reveal a splitting of peaks also in this case.

A reason for enhanced electrical conductivity in S930 films was investigated using cAFM. In order to find areas with an increased conductivity compared to the PFN–30BFO matrix, three secondary phases, namely the Pb/Bi-rich, Fe-rich and Fe/Cu-rich phases (Fig. 3(c–e)), were considered for the investigation. Since the cAFM measurements can only be performed on the surface of the thick films, as explained in Supplementary material H, we first tried to locate these three secondary phases on the sample surface using an SEM microscope. Only the Fe/Cu-rich phase was detected on the surface of the films in a small amount and at only one location. Therefore, the cAFM analysis was performed at this location, as shown schematically in Fig. 9(a). The SEM image with the corresponding AFM deflection image and the cAFM local electrical current image of the investigated location are shown in Fig. 9(b–d). The cAFM results reveal an increased electrical conductivity of the Fe/Cu-rich secondary phase with local electrical currents of up to 10 pA. No cAFM signal is detected in the matrix, indicating that its conductivity is below the detection limit of the instrument. For our instrument (AFM, MFP-3D, Asylum Research, USA, ORCA module), the measured RMS current noise is below 1 pA, specifically in the range of a few hundred femtoamperes [59]. This indicates that the enhancement in electrical conductivity in S930 films can be attributed to the presence of a conductive Fe/Cu-rich secondary phase. Other two secondary phases, namely the Pb/Bi-rich and Fe-rich phases, might also contribute to an enhanced conductivity of the S930 films, but since we could not observe them on the films surface, it was not possible to perform cAFM analysis on them. Furthermore, the electrical conductivity of the matrix was investigated in more detail. Literature [60] reports the impact of the different electrical conductivity of the grain boundaries compared with the grains on the electrical properties of the $0.67BiFeO_3$–$0.33BaTiO_3$ samples. However, our results show that both the grain boundaries and the domain walls exhibit no enhanced (or reduced) electrical conductivity compared to that of the matrix; therefore, we can probably exclude their major impact on the electrical properties of the samples. Details can be found in Supplementary material I.

The DBS of thick films was determined by applying an increasing DC voltage to the samples. The Weibull distribution of the measured dielectric breakdown fields (E_B) is shown in Fig. 10. The details on the determination of DBS can be found in Supplementary material J. The DBS of the S800 films (marked in red in Fig. 10) is the highest, namely 433 $kV{\cdot}cm^{-1}$, which is in agreement with the results obtained by measuring the *P–E* hysteresis loops, where the S800 films survived the highest electric field, namely 350 $kV{\cdot}cm^{-1}$. This is more than 100 $kV{\cdot}cm^{-1}$ higher than for the S850 films (marked in green in Fig. 10), which have a DBS of 304 $kV{\cdot}cm^{-1}$. The DBS of the S930 films (marked in blue in Fig. 10) is the lowest, namely 228 $kV{\cdot}cm^{-1}$. The results can be correlated with the grain size of the samples (Fig. 2); namely, the highest DBS is obtained in the films with the smallest grain size, as previously reported in [61–63]. In the S930 films, the Fe/Cu-rich secondary phase, which is more electrically conductive than the PFN–30BFO matrix (Fig. 9), contributes to the lower DBS of these films compared to the S800 and S850 films.

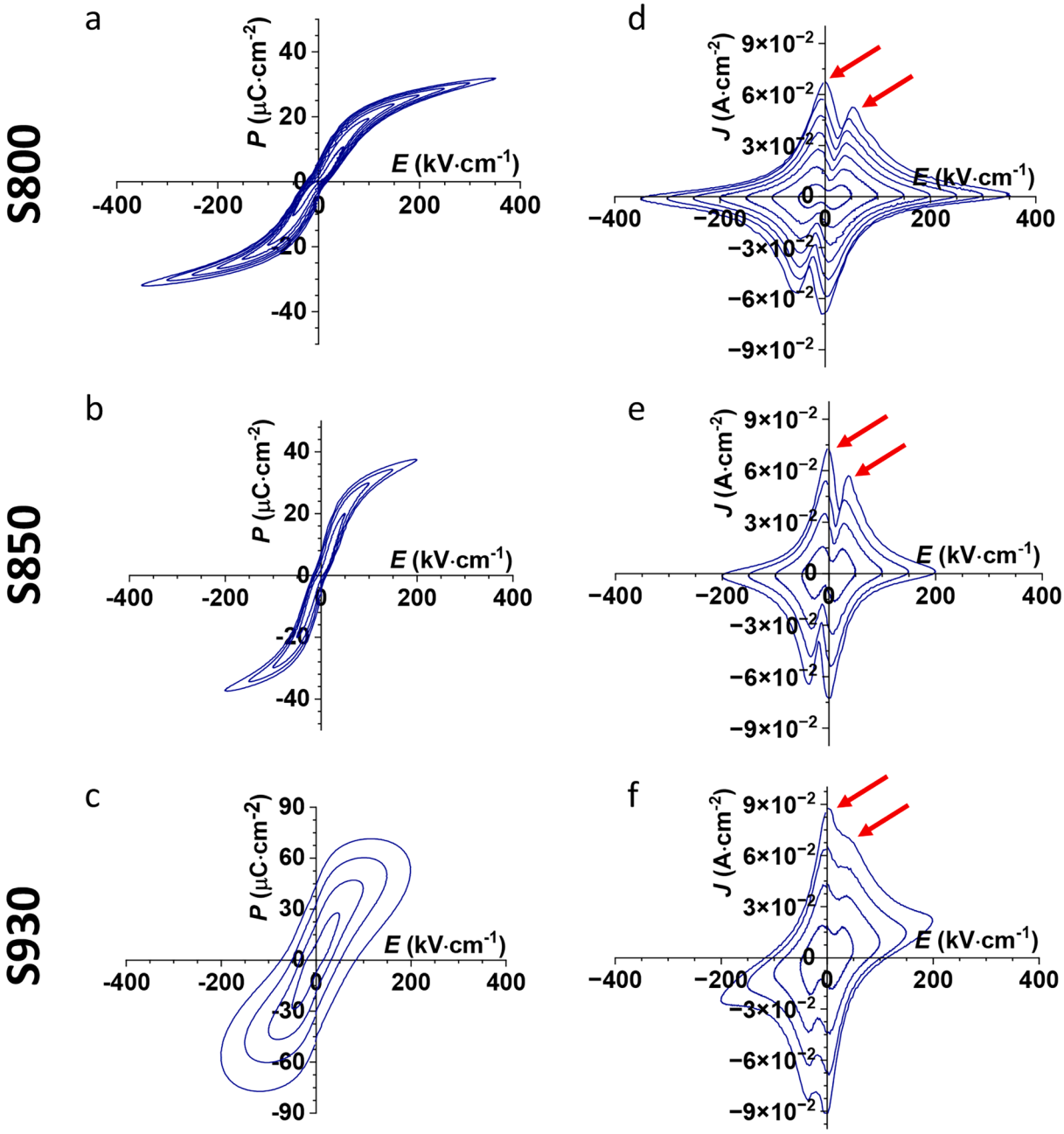

Fig. 8. Bipolar *P–E* hysteresis loops of (a) S800, (b) S850 and (c) S930 films. *J–E* hysteresis loops of (d) S800, (e) S850 and (f) S930 films. Red arrows indicate double current peaks.

4. Conclusions

In this work, PFN–30BFO thick films were successfully prepared by screen-printing method and sintered at 800 °C, 850 °C and 930 °C. The sintering temperature had no impact on the crystal structure of the thick films, which is pseudocubic indexed with the space group *Pm*-3*m* at RT. As the sintering temperature increased, the average grain size grew from ~0.6 μm for S800 to ~1.0 μm and ~2.2 μm for S850 and S930 films, respectively.

The maximum dielectric permittivity values of the S800, S850 and S930 films were determined to be ~2000 and ~4000 and ~4000, respectively. All thick films exhibited a broad frequency dependent permittivity peak. Piezoresponse force microscopy revealed clusters of polar nanoregions at both lower (0.1 V) and higher (2 V) voltages at RT, which is an indication of a relaxor-like behaviour in the films. In addition, wedge-like and irregularly- shaped ferroelectric domains were also observed at 2 V.

The peak permittivity temperatures of the thick films were found to be lower than those of the PFN–30BFO bulk ceramic. This shift can be attributed to the residual stresses formed in the films during the thermal treatment. To estimate the stresses, the thermal expansion coefficient of PFN–30BFO was measured and found to be ~$11 \cdot 10^{-6}$ K^{-1}. Further calculations showed that tensile stresses with a maximum value of ~70 MPa (at 100 °C) were formed in the films during cooling part of the sintering process.

The S800 and S850 films showed well-developed polarization versus electric field hysteresis loops compared to the S930 films, which exhibited round hysteresis loops due to excessive electrical conductivity. This excessive electrical conductivity was attributed to the Fe/Cu-rich phase that showed an increased electrical conductivity compared to

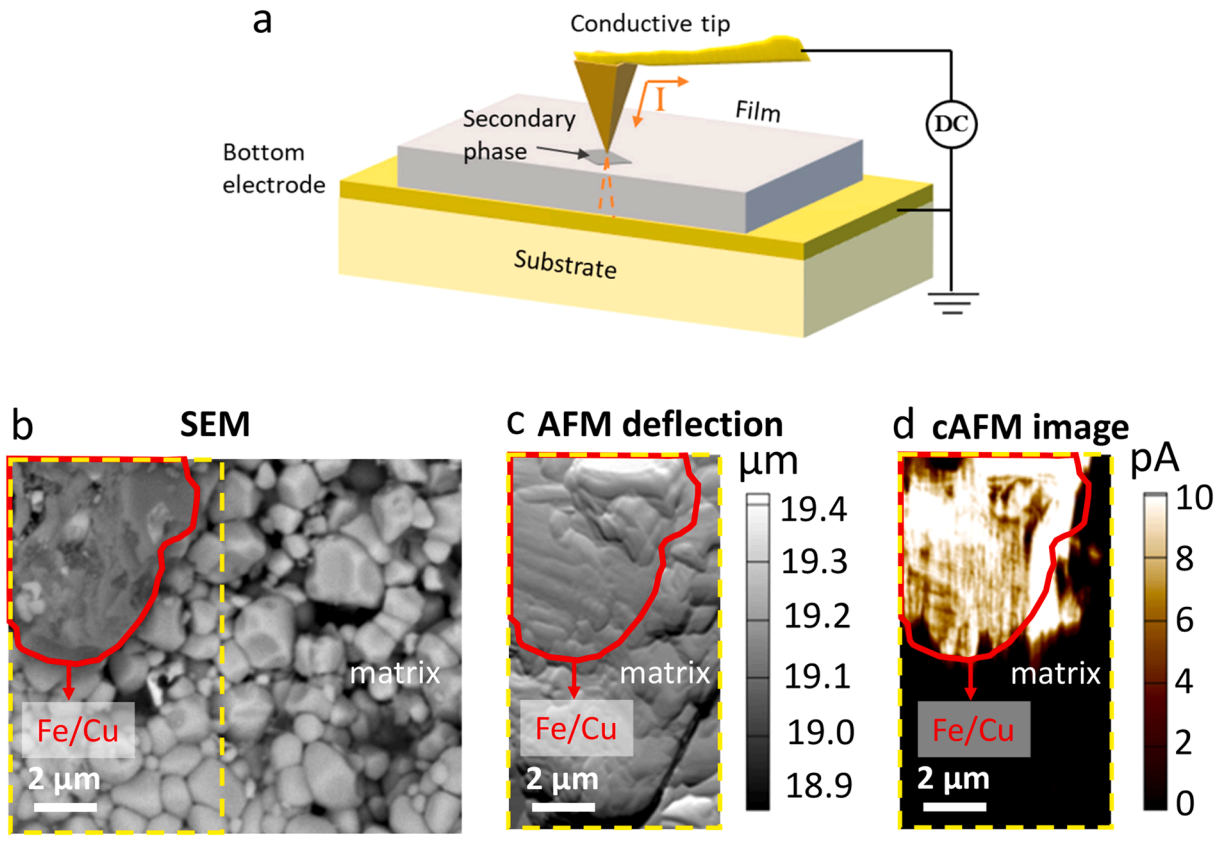

Fig. 9. (a) Schematic representation of the experimental setup for the cAFM measurements, (b) SEM microstructure, (c) AFM topography deflection image and (d) cAFM image of the Fe/Cu-rich secondary phase on the surface of the S930 films. The solid red lines are only a guide for the eyes, marking the border of the Fe/Cu-rich secondary phase. The dashed yellow boxes indicate an area studied by cAFM.

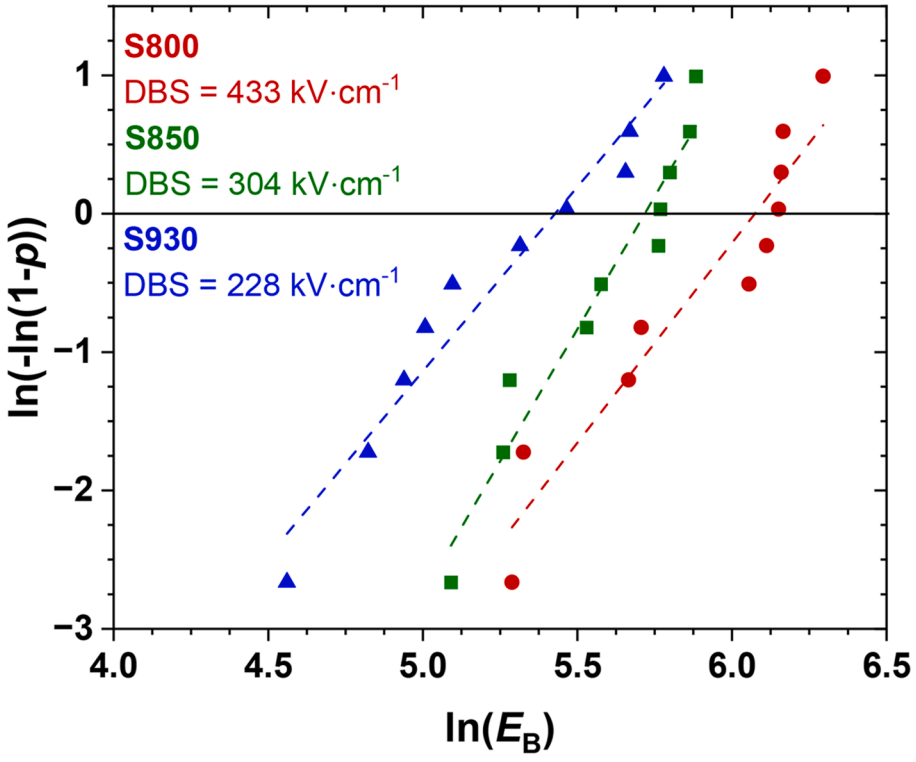

Fig. 10. Weibull distribution of the measured E_B of S800 (red dots), S850 (green squares) and S930 films (blue triangles). p is the cumulative failure probability. The dashed lines belong to the linear regression. The solid black line at $\ln(-\ln(1-p)) = 0$ is needed to determine the DBS.

the film matrix. For this reason and due to the largest grain size, these films had the lowest dielectric breakdown strength among the prepared thick films, i.e., 228 kV·cm^{-1}. Due to the smallest grain size, the highest dielectric breakdown strength was determined for the S800 films, namely 433 kV·cm^{-1}, which is more than 100 kV·cm^{-1} higher than that of the S850 films.

In conclusion, to achieve screen-printed PFN–30BFO thick films with optimal functionality, the films should be sintered at a low temperature, namely 800 °C. This results in low electrical conductivity and small grain size, leading to high dielectric breakdown strength. These films could be promising for future electronic device applications, particularly those requiring high dielectric breakdown strength.

CRediT authorship contribution statement

Ivana Goričan: Writing – review & editing, Writing – original draft, Visualization, Methodology, Investigation, Formal analysis, Data curation, Conceptualization. **Andreja Benčan:** Writing – review & editing, Methodology, Investigation, Data curation. **Silvo Drnovšek:** Methodology, Investigation, Data curation. **Antonio Iacomini:** Writing – review & editing, Methodology, Investigation, Data curation. **Nejc Suban:** Writing – review & editing, Methodology, Investigation, Data curation. **Brigita Kmet:** Methodology, Investigation, Data curation. **Uroš Prah:** Writing – review & editing, Methodology, Investigation, Data curation. **Tadej Rojac:** Writing – review & editing, Writing – original draft, Supervision, Methodology, Investigation, Data curation, Conceptualization. **Hana Uršič:** Writing – review & editing, Writing – original draft, Supervision, Methodology, Investigation, Funding acquisition, Conceptualization.

Declaration of Competing Interest

The authors declare that they have no known competing financial interests or personal relationships that could have appeared to influence the work reported in this paper.

Acknowledgements

This work was supported by the Slovenian Research and Innovation Agency (research project N2-0212, research core funding P2-0105 and Young Researcher project). Matej Šadl, Jena Cilenšek, Jennifer Oktaviany and Teodora Vujić are gratefully acknowledged for their help in the laboratory.

Appendix A. Supporting information

Supplementary data associated with this article can be found in the online version at doi:10.1016/j.jeurceramsoc.2026.118317.

Data availability

The data that support the findings of this study are available at Zenodo repository [64].

References

[1] R.A. Dorey, Ceramic Thick Films for MEMS and Microdevices, Elsevier, United Kingdom, 2012 (ISBN 978-1-4377-7817-5).
[2] B. Malic, D. Kuscer, M. Vrabelj, J. Koruza, Review of methods for powder-based processing, in: G. Korotcenkov (Ed.), Chapter 5 in the Book Magnetic, Ferroelectric, and Multiferroic Metal Oxides, Elsevier, 2018 (ISBN 978-0-12-811180-2).
[3] M. Kosec, D. Kuscer, J. Holc, Processing of ferroelectric ceramic thick films, in: L. Pardo, A. Ricote (Eds.), Chapter 2 in the Book Multifunctional Polycrystalline Ferroelectric Materials – Processing and Properties, Springer, 2011 (ISBN 978-90-481-2874-7).
[4] U. Prah, M. Dragomir, T. Rojac, A. Benčan, R. Broughton, C.-C. Chung, J.L. Jones, R. Sherbondy, G. Brennecka, H. Uršič, Strengthened relaxor behavior in (1–x)Pb($Fe_{0.5}Nb_{0.5}$)O_3–$x$$BiFeO_3$, J. Mater. Chem. C 8 (10) (2020) 3452–3462, https://doi.org/10.1039/c9tc05883d.
[5] N. Lampis, P. Sciau, A.G. Lehmann, Rietveld refinements of the paraelectric and ferroelectric structures of $PbFe_{0.5}Nb_{0.5}O_3$, J. Phys. Condens. Matter 11 (17) (1999) 3489–3500, https://doi.org/10.1088/0953-8984/11/17/307.
[6] H. Ursic, A. Bencan, U. Prah, M. Dragomir, B. Malic, Structure and dynamics of ferroelectric domains in polycrystalline Pb($Fe_{1/2}Nb_{1/2}$)O_3, Mater 12 (8) (2019), https://doi.org/10.3390/ma12081327.
[7] C.F. Buhrer, Some properties of bismuth perovskites, J. Chem. Phys. 36 (3) (1962) 798–803, https://doi.org/10.1063/1.1732613.
[8] J.M. Moreau, C. Michel, R. Gerson, W.J. James, Ferroelectric $BiFeO_3$ X-ray and neutron diffraction study, J. Phys. Chem. Solids 32 (6) (1971) 1315–1320, https://doi.org/10.1016/S0022-3697(71)80189-0.
[9] N.N. Krainik, N.P. Khuchua, A.A. Berezhnoi, A.G. Tutov, Nature of phase transformations in solid solutions of $BiFeO_3$ with $PbFe_{1/2}Nb_{1/2}O_3$, Sov. Phys. Solid State 7 (1965) 100–107.
[10] H. Li, J. Zhuang, A.A. Bokov, N. Zhang, J. Zhang, W. Ren, Z.-G. Ye, Coexistence of relaxor behavior and ferromagnetic order in multiferroic Pb($Fe_{0.5}Nb_{0.5}$)O_3–$BiFeO_3$ solid solution, J. Mater. Chem. C 8 (38) (2020) 13306–13318, https://doi.org/10.1039/d0tc03505j.
[11] G.A. Smolenskii, V.M. Yudin, Weak ferromagnetism of some $BiFeO_3$–Pb($Fe_{0.5}Nb_{0.5}$)O_3 perovskites, Sov. Phys. Solid State 6 (1965) 2936–2942.
[12] D. Viehland, S.J. Jang, L.E. Cross, M. Wuttig, Freezing of the polarization fluctuations in lead magnesium niobate relaxors, J. Appl. Phys. 68 (1990) 2916–2921, https://doi.org/10.1063/1.346425.
[13] U. Prah, T. Rojac, M. Wencka, M. Dragomir, A. Bradeško, A. Benčan, R. Sherbondy, G. Brennecka, Z. Kutnjak, B. Malič, H. Uršič, Improving the multicaloric properties of Pb($Fe_{0.5}Nb_{0.5}$)O_3 by controlling the sintering conditions and doping with manganese, J. Eur. Ceram. Soc. 39 (14) (2019) 4122–4130, https://doi.org/10.1016/j.jeurceramsoc.2019.05.062.
[14] R. Mackeviciute, V. Goian, S. Greicius, R. Grigalaitis, D. Nuzhnyy, J. Holc, J. Banys, S. Kamba, Lattice dynamics and broad-band dielectric properties of multiferroic Pb($Fe_{1/2}Nb_{1/2}$)O_3 ceramics, J. Appl. Phys. 117 (8) (2015), https://doi.org/10.1063/1.4913286.
[15] U. Prah, M. Wencka, T. Rojac, A. Benčan, H. Uršič, Pb($Fe_{0.5}Nb_{0.5}$)O_3–$BiFeO_3$-based multicalorics with room-temperature ferroic anomalies, J. Mater. Chem. C 8 (32) (2020) 11282–11291, https://doi.org/10.1039/d0tc02329a.
[16] D. Bochenek, P. Niemiec, P. Guzdek, M. Wzorek, Magnetoelectric and electric measurements of the (1−x)$BiFeO_3$–(x)Pb($Fe_{1/2}Nb_{1/2}$)O_3 solid solutions, Mater. Chem. Phys. 195 (2017) 199–206, https://doi.org/10.1016/j.matchemphys.2017.04.022.
[17] T. Rojac, A. Bencan, B. Malic, G. Tutuncu, J.L. Jones, J.E. Daniels, D. Damjanovic, $BiFeO_3$ ceramics: processing, electrical, and electromechanical properties, J. Am. Ceram. Soc. 97 (7) (2014) 1993–2011, https://doi.org/10.1111/jace.12982.
[18] W.N. Su, D.H. Wang, Q.Q. Cao, Z.D. Han, J. Yin, J.R. Zhang, Y.W. Du, Large polarization and enhanced magnetic properties in $BiFeO_3$ ceramic prepared by high-pressure synthesis, Appl. Phys. Lett. 91 (9) (2007), https://doi.org/10.1063/1.2776864.
[19] T. Rojac, M. Makarovic, J. Walker, H. Ursic, D. Damjanovic, T. Kos, Piezoelectric response of $BiFeO_3$ ceramics at elevated temperatures, Appl. Phys. Lett. 109 (4) (2016), https://doi.org/10.1063/1.4960103.
[20] R. Havlicek, J.P. Vejpravova, D. Bochenek, Structure and magnetic properties of perovskite-like multiferroic $PbFe_{0.5}Nb_{0.5}O_3$, J. Phys. Conf. Ser. 200 (2010) 012058, https://doi.org/10.1088/1742-6596/200/1/012058 (1–4).
[21] V.V. Laguta, J. Rosa, L. Jastrabik, R. Blinc, P. Cevc, B. Zalar, M. Remskar, S. I. Raevskaya, I.P. Raevski, ^{93}Nb NMR and Fe^{3+} EPR study of local magnetic properties of magnetoelectric Pb($Fe_{1/2}Nb_{1/2}$)O_3, Mater. Res. Bull. 45 (2010) 1720–1727, https://doi.org/10.1016/j.materresbull.2010.06.060.
[22] G.A. Smolenskii, I.E. Chupis, Ferroelectromagnets, Sov. Phys. Uspekhi 25 (1982) 475–493, https://doi.org/10.1070/PU1982v025n07ABEH004570.
[23] A.V. Pavlenko, V.G. Smotrakov, S.P. Kubrin, L.A. Shilkina, V.V. Eremkin, S. I. Shevtsova, L.A. Reznichenko, Preparation, structure, and dielectric characteristics of 0.95PFN–0.05BFO single crystals, Bull. Russ. Acad. Sci. Phys. 81 (3) (2017) 334–336, https://doi.org/10.3103/S1062873817030261.
[24] K.M. Zhidel, A.V. Pavlenko, Preparation and properties of 0.5$BiFeO_3$–0.5$PbFe_{0.5}Nb_{0.5}O_3$ ceramics and polycrystalline films, J. Adv. Dielectr. 12 (1) (2022), https://doi.org/10.1142/S2010135X2160002X.
[25] H. Uršič, M. Hrovat, J. Holc, J. Tellier, S. Drnovšek, N. Guiblin, B. Dkhil, M. Kosec, Influence of the substrate on the phase composition and electrical properties of 0.65PMN–0.35PT thick films, J. Eur. Ceram. Soc. 30 (10) (2010) 2081–2092, https://doi.org/10.1016/j.jeurceramsoc.2010.04.010.
[26] M. Kosec, J. Holc, B. Malič, V. Bobnar, Processing of high performance lead lanthanum zirconate titanate thick films, J. Eur. Ceram. Soc. 19 (6–7) (1999) 949–954, https://doi.org/10.1016/S0955-2219(98)00351-3.
[27] H. Uršič, A. Benčan, E. Khomyakova, S. Drnovšek, I.F. Mercioniu, K. Makarovič, D. Belavič, C. Schreiner, R. Ciobanu, P. Fanjul Bolado, B. Malič, Pb(Mg,Nb)O_3–$PbTiO_3$ thick films on metalized low-temperature co-fired ceramic substrates, Inf. MIDEM 47 (2) (2017) 71–78.
[28] B. Mallesham, R. Ranjith, M. Manivelraja, Scandium induced structural transformation and B':B" cationic ordering in Pb($Fe_{0.5}Nb_{0.5}$)O_3 multiferroic ceramics, J. Appl. Phys. 116 (2014) 034104, https://doi.org/10.1063/1.4890020 (1–7).
[29] I.O. Troyanchuk, N.V. Tereshko, D.V. Karpinsky, A.L. Kholkin, M. Kopcewicz, K. Bärner, Enhanced piezoelectric and magnetic properties of $Bi_{1-x}Ca_xFe_{1-x/2}Nb_{x/2}O_3$ solid solutions, J. Appl. Phys. 109 (2011) 114102, https://doi.org/10.1063/1.3594251, 1-6.

[30] M. Bortolotti, L. Lutterotti, G. Pepponi, Combining XRD and XRF analysis in one Rietveld-like fitting, Powder Diffr. 32 (S1) (2017) S225–S230, https://doi.org/10.1017/S0885715617000276.
[31] W.H. Walton, Feret's statistical diameter as a measure of particle size, Nature 162 (1948) 329–330, https://doi.org/10.1038/162329B0.
[32] D. Wilcox, B. Dove, B. McDavid, D. Greer, UTHSCSA Image Tool for Windows Version 3.0, University of Texas Health Science Center, USA, 2002.
[33] B. Waloddi Weibull, A statistical distribution function of wide applicability, J. Appl. Mech. 18 (1951) 293–297.
[34] R.D. Abernethy, J.E. Breneman, C.H. Medlin, G.L. Reinman, Weibull Analysis Handbook. U. S. Air force AFWAL-TR-83-2079, 1983.
[35] E. Tuncer, D.Randy James, I. Sauers, A.R. Ellis, M.O. Pace, On dielectric breakdown statistics, J. Phys. D: Appl. Phys. 39 (19) (2006) 4257–4268, https://doi.org/10.1088/0022-3727/39/19/020.
[36] E. Khomyakova, J. Pavlic, M. Makarovic, H. Ursic, J. Walker, T. Rojac, B. Malic, A. Bencan, Integration of $BiFeO_3$ thick films onto ceramic and metal substrates by screen printing, J. Eur. Ceram. Soc. 35 (15) (2015) 4163–4171, https://doi.org/10.1016/j.jeurceramsoc.2015.07.001.
[37] R.M. Biefeld, S.S. White, Temperature/composition phase diagram of the system Bi_2O_3–PbO, J. Am. Ceram. Soc. 64 (3) (1970) 182–184, https://doi.org/10.1111/j.1151-2916.1981.tb10253.x.
[38] B.D. Cullity, S.R. Stock. Elements of X-ray Diffraction, Third edition, Pearson, United Kingdom, 2014 (ISBN 978-1-292-04054-7).
[39] S. Singh, A. Kaur, P. Kaur, L. Singh, High-temperature dielectric relaxation and electric conduction mechanisms in a $LaCoO_3$-modified $Na_{0.5}Bi_{0.5}TiO_3$ system, ACS Omega 8 (2023) 25623–25638, https://doi.org/10.1021/acsomega.3c04490.
[40] J. Xu, M. Itoh, Unusual dielectric relaxation in lightly doped n-type rhombohedral $BaTi_{0.85}Zr_{0.15}O_3$:Ta ferroelectric ceramics, Chem. Mater. 17 (2005) 1711–1716, https://doi.org/10.1021/cm050145a.
[41] S.A. Mazen, H.M. Zaki, Effect of tetra ionic substitution on the dielectric properties of Cu-ferrite, Phys. Stat. Sol. A 199 (2003) 305–320, https://doi.org/10.1002/pssa.200306638.
[42] M. Algueró, J. Ricote, R. Jiménez, P. Ramos, J. Carreaud, B. Dkhil, J.M. Kiat, J. Holc, M. Kosec, Size effect in morphotropic phase boundary $Pb(Mg_{1/3}Nb_{2/3})O_3$–$PbTiO_3$, Appl. Phys. Lett. 91 (2007) 112905, https://doi.org/10.1063/1.2778471 (1–3).
[43] M. Sadl, U. Prah, V. Kovacova, E. Defay, T. Rojac, A. Lebar, J. Valentinčič, H. Ursic, Multifunctional flexible ferroelectric thick-film structures with energy storage, piezoelectric and electrocaloric performance, J. Mater. Chem. C 11 (2023) 10058–10068, https://doi.org/10.1039/d3tc01555f.
[44] H. Amorín, M. Venet, J.E. García, D.A. Ochoa, P. Ramos, J. López-Sánchez, J. Rubio-Zuazo, A. Castro, M. Algueró, Insights into the early size effects of lead-free piezoelectric $Ba_{0.85}Ca_{0.15}Zr_{0.1}Ti_{0.9}O_3$, Adv. Electron. Mater. 10 (2024) 2300556, https://doi.org/10.1002/aelm.202300556 (1–12).
[45] S. Merselmiz, I. Goričan, T. Rojac, V. Bobnar, V. Regis, M. Šadl, V. Fišinger, N. Suban, B. Kmet, A. Benčan, A. Bradeško, A. Debevec, B. Malič, H. Uršič, Capacitive energy-storage and electromechanical properties of aerosol-deposited $0.5BaZr_{0.2}Ti_{0.8}O_3$–$0.5Ba_{0.7}Ca_{0.3}TiO_3$ films, Acta Mater. 304 (2026) 121749, https://doi.org/10.1016/j.actamat.2025.121749 (1–12).
[46] J. Carreaud, P. Gemeiner, J.M. Kiat, B. Dkhil, C. Bogicevic, T. Rojac, B. Malic, Size-driven relaxation and polar states in $PbMg_{1/3}Nb_{2/3}O_3$-based system, Phys. Rev. B 72 (2005) 174115, https://doi.org/10.1103/PhysRevB.72.174115 (1–6).
[47] R. Jiménez, H. Amorín, J. Ricote, J. Carreaud, J.M. Kiat, B. Dkhil, J. Holc, M. Kosec, M. Algueró, Effect of grain size on the transition between ferroelectric and relaxor states in $0.8Pb(Mg_{1/3}Nb_{2/3})O_3$–$0.2PbTiO_3$ ceramics, Phys. Rev. B 78 (2008) 094103, https://doi.org/10.1103/PhysRevB.78.094103 (1–9).
[48] T. Hungría, H. Amorín, M. Algueró, A. Castro, Nanostructured ceramics of $BiScO_3$–$PbTiO_3$ with tailored grain size by spark plasma sintering, Scr. Mater. 64 (2011) 97–100, https://doi.org/10.1016/j.scriptamat.2010.09.023.
[49] M. Ohring, The Materials Science of Thin Films, Academic Press, USA, 1992 (ISBN 0-12-524990).
[50] M. Kuhfuß, U.R. Eckstein, D. Urushihara, T. Asaka, L. Xie, A. Martin, K. Kakimoto, K.G. Webber, Temperature-dependent residual stress in aerosol-deposited barium titanate films, Ceram. Int. 51 (2025) 48397–48408, https://doi.org/10.1016/j.ceramint.2025.08.093.
[51] L. Zia, G.H. Jaffari, R. Jiménez, I. Bretos, H. Amorín, M. Algueró, E. Rodríguez-Castellón, M.L. Calzada, Solution processing of morphotropic phase boundary $BiFeO_3$–$PbTiO_3$ thin films with reduced conductivity for high room-temperature switchable polarization, J. Am. Ceram. Soc. 105 (2022) 888–900, https://doi.org/10.1111/jace.18158.
[52] G. Han, J. Ryu, W.H. Yoon, J.J. Choi, B.D. Hahn, J.W. Kim, D.S. Park, C.W. Ahn, S. Priya, D.Y. Jeong, Stress-controlled $Pb(Zr_{0.52}Ti_{0.48})O_3$ thick films by thermal expansion mismatch between substrate and $Pb(Zr_{0.52}Ti_{0.48})O_3$ film, J. Appl. Phys. 110 (2011) 124101, https://doi.org/10.1063/1.3669384 (1–5).
[53] N.H. Khansur, U. Eckstein, L. Benker, U. Deisinger, B. Merle, K.G. Webber, Room temperature deposition of functional ceramic films on low-cost metal substrate, Ceram. Int. 44 (2018) 16295–16301, https://doi.org/10.1016/j.ceramint.2018.06.027.
[54] J. Zygmuntowicz, M. Piatek, A. Miazga, K. Konopka, W. Kaszuwara, Dilatrometric sintering study and characterization of alumina–nickel composites, Process. Appl. Ceram. 12 (2018) 111–117, https://doi.org/10.2298/PAC1802111Z.
[55] D.B. Marghitu, C.I. Diaconescu, B.O. Ciocirlan, Mechanics of materials, in: Dan B. Marghitu (Ed.), Chapter 3 in book Mechanical Engineer's Handbook, Academic Press, 2001.
[56] V.V. Shvartsman, A.L. Kholkin, Investigation of the ferroelectric-relaxor transition in $PbMg_{1/3}Nb_{2/3}O_3$–$PbTiO_3$ ceramics by piezoresponse force microscopy, J. Appl. Phys. 108 (2010) 042007, https://doi.org/10.1063/1.3474962 (1–6).
[57] J. Dec, W. Kleemann, V.V. Shvartsman, D.C. Lupascu, T. Ukasiewicz, From mesoscopic to global polar order in the uniaxial relaxor ferroelectric $Sr_{0.8}Ba_{0.2}Nb_2O_6$, Appl. Phys. Lett. 100 (2012) 052903, https://doi.org/10.1063/1.3680599 (1–4).
[58] L. Gimadeeva, A. Ushakov, A. Pugachev, A. Turygin, R. Jing, Q. Hu, X. Wei, Z. Hu, V. Shur, L. Jin, D. Alikin, Mesoscale mechanisms of the diffuse dielectric behaviour and retention of the polar nano-regions in the polycrystalline ferroelectric $BaTiO_3$, J. Mater. 11 (2025) 101014, https://doi.org/10.1016/j.jmat.2025.101014 (1–10).
[59] Oxford Instruments, Asylum Research, ORCA™ – Conductive AFM Imaging Using the MFP-3D™ AFM.
[60] A. Iacomini, M. Koblar, H. Uršič, T. Rojac, Tuning the electrical conductivity and Maxwell-Wagner relaxation in $BiFeO_3$–$BaTiO_3$ piezoceramics, J. Eur. Ceram. Soc. 44 (2024) 6948–6959, https://doi.org/10.1016/j.jeurceramsoc.2024.04.046.
[61] T. Tunkasiri, G. Rujijanagul, Dielectric strength of fine grained barium titanate ceramics, J. Mater. Sci. Lett. 15 (1996) 1767–1769, https://doi.org/10.1007/BF00275336.
[62] K. Yamashita, K. Koumoto, M. Takata, H. Yanagida, Statistical analysis of dielectric strength of $BaTiO_3$ ceramic films, Jpn. J. Appl. Phys. 19 (1980) 867–871, https://doi.org/10.1143/JJAP.19.867.
[63] H.Y. Lee, K.H. Cho, H.D. Nam, Grain size and temperature dependence of electrical breakdown in $BaTiO_3$ ceramic, Ferroelectrics (2006) 165–169, https://doi.org/10.1080/00150190600694415.
I. Goričan, H. Uršič, Impact of sintering temperature on structural, microstructural and electrical properties of screen-printed $0.7Pb(Fe_{0.5}Nb_{0.5})O_3$–$0.3BiFeO_3$ thick films, Zenodo, 2025, https://doi.org/10.5281/zenodo.17818575.